Diamond & Related Materials 20 (2011) 641–650

Contents lists available at ScienceDirect

Diamond & Related Materials

journal homepage: www.elsevier.com/locate/diamond

Diamond growth on WC-Co substrates by hot filament chemical vapor deposition: Effect of filament–substrate separation

Qiuping Wei [a,b,c], Michael N.R. Ashfold [b], Yu. A. Mankelevich [d], Z.M. Yu [a,*], P.Z. Liu [a], L. Ma [c]

[a] School of Materials Science and Engineering, Central South University, Changsha, 410083, PR China
[b] School of Chemistry, University of Bristol, Bristol BS8 1TS, United Kingdom
[c] State Key Laboratory of Powder Metallurgy, Central South University, Changsha, 410083, PR China
[d] Skobel'tsyn Institute of Nuclear Physics, Moscow State University, Leninskie gory, Moscow 119991, Russia

ARTICLE INFO

Article history:
Received 20 August 2010
Received in revised form 3 December 2010
Accepted 28 February 2011
Available online 11 March 2011

Keywords:
CVD diamond films
Hot filament chemical vapor deposition (HFCVD)
Filament–substrate distance
Raman spectroscopy
Gas phase modeling

ABSTRACT

Polycrystalline diamond films have been grown by hot filament (HF) chemical vapor deposition on WC-Co bar substrates using different CH_4/H_2 source gas mixing ratios and two different total gas pressures. Each substrate was mounted so as to span a range of HF-substrate separations, d_f, (and thus substrate temperatures) and therefore samples a spread of incident gas phase chemistry and compositions. Spatially resolved scanning electron microscopy and Raman analysis of the deposited material provides a detailed picture of the evolution of film morphology, growth rate, sp^3/sp^2 content and stress with d_f in each deposited sample, and of how these properties vary with process conditions. The experimental study is complemented by two-dimensional model calculations of the HF-activated gas phase chemistry and composition, which succeeds in reproducing the measured growth rates well.

1. Introduction

Chemical vapor deposition (CVD) from activated hydrocarbon/H_2 gas mixtures is an established technique for growing hard, wear-resistant polycrystalline diamond films on a range of substrates (tungsten, molybdenum, silicon, etc.) [1–4]. Successful diamond deposition requires elevated substrate temperatures (T_s>700 °C). The thermal expansion coefficient of diamond (0.9 ppm K^{-1}) [5] is much smaller than that of the favored substrate materials. Typically, therefore, CVD diamond coatings contain (compressive) stress which, in many cases, will lead to delamination from the substrate. The favored substrates (W, Mo, Si, etc.) each have a tendency to form an interfacial carbide layer under standard CVD conditions which serves as a barrier layer, limiting carburization (the dissolution of carbon from the process gas mixture into the bulk of the substrate) and providing some stress relief at the interface.

Carburization has been a longstanding challenge to the diamond coating of steel substrates. We have recently reported hot filament (HF) assisted CVD of adherent diamond films on steel substrates that had themselves been pre-coated with a thin WC-Co interlayer [6]. Successful diamond growth was achieved after pre-treating the WC-Co interlayer with a two stage etching process, which had the effect of depleting the Co content at the surface. Diamond growth was shown to be accompanied by some additional carburization of the pre-treated WC interlayer, which encourages film adhesion. We also investigated a range of pre-treatment methods for diamond films deposited on sintered WC-Co substrates with different cobalt contents [7,8]. Here we report more extensive investigations of HFCVD of diamond films on large ($22\times6\times5$ mm^3) pre-treated WC-6% wt Co substrates, as a function of C/H ratio in the process gas mixture. Each substrate is mounted so as to span a range of distances d_f from the HF. T_s in the present work is determined by a combination of radiative and conductive heat transfer from the HF, and by the exothermicity of H atom recombination on the substrate surface. The present arrangement thus ensures that growth on different regions of the substrate surface samples different T_s and a different mix of incident gas phase species. The variations in incident gas phase reactant densities can be predicted on the basis of earlier diagnosis and modeling of HF activated CH_4/H_2 gas mixtures [9–13]. Here we attempt to relate variations in the growth rates and quality of diamond films grown on WC (a substrate selected for its comparative stability under CVD processing conditions), with different CH_4/H_2 mixing ratio, total gas pressure and d_f, with theoretically predicted variations in the gas phase and gas-surface process conditions.

2. Experimental details

WC-6% wt Co bars (Zhuzhou Cemented Carbide Group Corporation, Hunan, China) with a dimension of $22\times6\times5$ mm^3 were used as

* Corresponding author. Tel.: +86 731 8830335; fax: +86 731 8876692.
E-mail addresses: zhiming@mail.csu.edu.cn, qpweicsu@gmail.com (Z.M. Yu).

0925-9635/$ – see front matter © 2011 Elsevier B.V. All rights reserved.
doi:10.1016/j.diamond.2011.02.017

the substrates. Each specimen was first subjected to the following two-step pretreatment: (i) etching of tungsten carbide by Murakami's reagent (10 g $K_3[Fe(CN)_6]$ + 10 g KOH + 100 ml H_2O) for 5 min in an ultrasonic vessel [14]; (ii) removal of the surface Co by etching in an acidic solution of hydrogen peroxide (2 ml 96% wt H_2SO_4 + 2 ml 68% wt HNO_3 + 2 ml 45% wt HCl + 10 ml 40% w/v H_2O_2 + 20 ml H_2O) for 5 min. Prior to diamond deposition, all pretreated specimens were then abraded ultrasonically in a suspension of diamond powder (<500 nm particle size) in acetone for 30 min. Ultrasonic agitation serves to disperse the nanodiamond powder in the acetone and to enhance collisions of diamond particles with the substrate. This treatment, often described as 'seeding' [1,4], encourages the subsequent inhomogeneous nucleation of diamond during CVD — either by implanting ultrafine diamond fragments into the substrate surface, or by creating suitable surface defects. The substrate samples were subsequently cleaned ultrasonically with acetone and ethanol for 3 min after seeding.

The diamond films were synthesized by HFCVD in a multifunctional vapor deposition system specially designed for diamond deposition. It consists of a gas handling system, a reactor, and a gas sampling and analysis system linked to vacuum pumps. The reactor is a stainless steel chamber with an inner diameter of 300 mm to which are fitted various electrical, gas and liquid feed-throughs, as well as a magnetron cathode for sputtering. A linear motion feed-through allowed in situ control of the filament–substrate distance. A spiral coil filament (tungsten wire, diameter 0.38 mm, screw inner diameter 1 mm, 14 turns, 1 mm separation between adjacent turns, coil length 14 mm), suspended between two molybdenum rods that are themselves mounted on water cooled copper frames, was used to activate the process gas for diamond film deposition. The power to the filament was supplied from a dc supply (operating in current limited mode) via an electrical feed-through. The substrate was positioned at an angle of ~30° to the vertical (z axis) as shown in Fig. 1. The filament temperature (T_f) was measured using an optical pyrometer. The temperature of the substrate surface (T_s) was controlled by T_f and the filament to substrate distance, d_f. T_s was measured with two K-type thermocouples attached to opposite edges of the substrate. The base pressure ($<1\times10^{-6}$ Torr) was maintained by a turbomolecular pump, and the deposition pressure, p, monitored and controlled using a manometer coupled to valve E on the vacuum line. Table 1 details the process parameters that were maintained constant for each deposition on each specimen. Key features to note here are that all specimens were grown using the same total gas flow rate (100 standard cm^3 per minute (sccm)), that specimens I and II involved the same (low) C/H input gas ratio but the pressure used in the former deposition is 2.5-times higher, and that specimens II–IV all involve a common p but different C/H input ratios (and some inevitable variations in power to the filament, in T_f and thus in T_s).

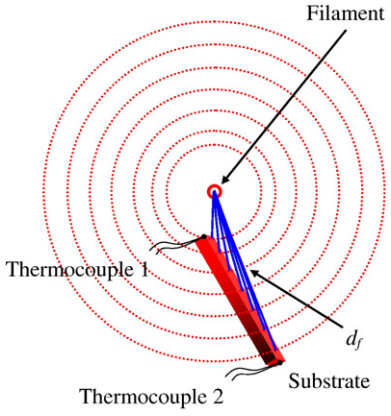

Fig. 1. Schematic illustration of the HF-substrate configuration.

Table 1
Experimental parameters used for diamond film deposition on WC-Co substrates.

Specimen no.	I	II	III	IV
Distance from filament to the top of substrate (mm)	6 ± 1	6 ± 1	6 ± 1	6 ± 1
Filament current (A)	20.7 ± 0.1	20.7 ± 0.1	20.7 ± 0.1	20.7 ± 0.1
Filament voltage (V)	24.5 ± 0.1	24.8 ± 0.1	25.2 ± 0.1	25.8 ± 0.1
Filament power (W)	507 ± 5	513 ± 5	522 ± 5	534 ± 5
Filament temperature (°C)	2180 ± 50	2210 ± 50	2240 ± 50	2300 ± 50
Substrate temperature nearest to HF (°C)	870 ± 30	880 ± 30	890 ± 30	900 ± 30
Substrate temperature furthest from HF (°C)	570 ± 20	590 ± 20	600 ± 20	610 ± 20
CH_4 flow rate (sccm)	1	1	2	4
H_2 flow rate (sccm)	99	99	98	96
Deposition pressure (kPa)	5.0	2.0	2.0	2.0
Deposition time (min)	180	180	180	180

The surface and cross-section morphologies of the as-grown diamond films were characterized at many different locations within each sample by SEM (FEI, Sirion200 Field-emission SEM and Quanta200 Environmental SEM), and their quality assessed by Raman spectroscopy (LabRAM HR800) at an excitation wavelength of 488 nm (argon ion laser, output power of 100 mW).

3. Results and discussion

3.1. Growth rate and morphology

SEM images of local areas of the surfaces of diamond films deposited under selected CVD conditions (specimens I, II and IV) are shown in the left hand panels of Fig. 2. The d_f distance (in mm) is shown at the upper left of each panel. As d_f increases from 6.0 mm to 21.6 mm, the SEM images of all specimens show the surface morphology evolving from a dense, homogeneous well-facetted, polycrystalline diamond film, through a 'cauliflower'-like morphology (at d_f ~ 10–12 mm), to an agglomeration of quasi-spherical nanoscale particles. Inspection of these images clearly shows the d_f dependence of the surface morphology to be more sensitive to the CH_4 flow rate, $F(CH_4)$, in the input gas feed (compare the images of specimens II–IV) than to the process gas pressure (from comparison of specimens I and II). The right hand panels in Fig. 2 show cross-sectional SEM images of diamond films deposited on specimens I, II and IV, measured at the d_f values (in mm) listed at the upper left of each image. Films grown under near optimal conditions (i.e. at short d_f , as for cross-section SEM image IV-6.0 in Fig. 2) show the characteristic columnar structure associated with good quality polycrystalline diamond films. As Fig. 3 shows, the growth rate, G, falls with increasing d_f under all process conditions. G scales roughly linearly with $F(CH_4)$ at small d_f (~6 mm) but is rather insensitive to $F(CH_4)$ at large d_f. As Table 1 shows, increasing $F(CH_4)$ under the present experimental conditions also causes some increase in T_f. This, in turn, is likely to cause some increase in the H atom density (and thus the CH_3 radical density in the near HF region), and some increase in T_s (particularly at small d_f) which can also contribute to an increased growth rate [15]. As with the surface morphology, G is relatively insensitive to the process gas pressure though, as Fig. 3 shows, the sample grown at higher p (specimen I) is consistently thinner than the specimen II sample grown at the same d_f.

3.2. Raman spectroscopy analysis

Raman spectroscopy is widely used within the diamond CVD community, given its ability to reveal the presence of different carbon phases (most notably diamond and graphite), and information concerning the average grain size and crystallinity within such domains. Films deposited on specimens I, II, III and IV were all

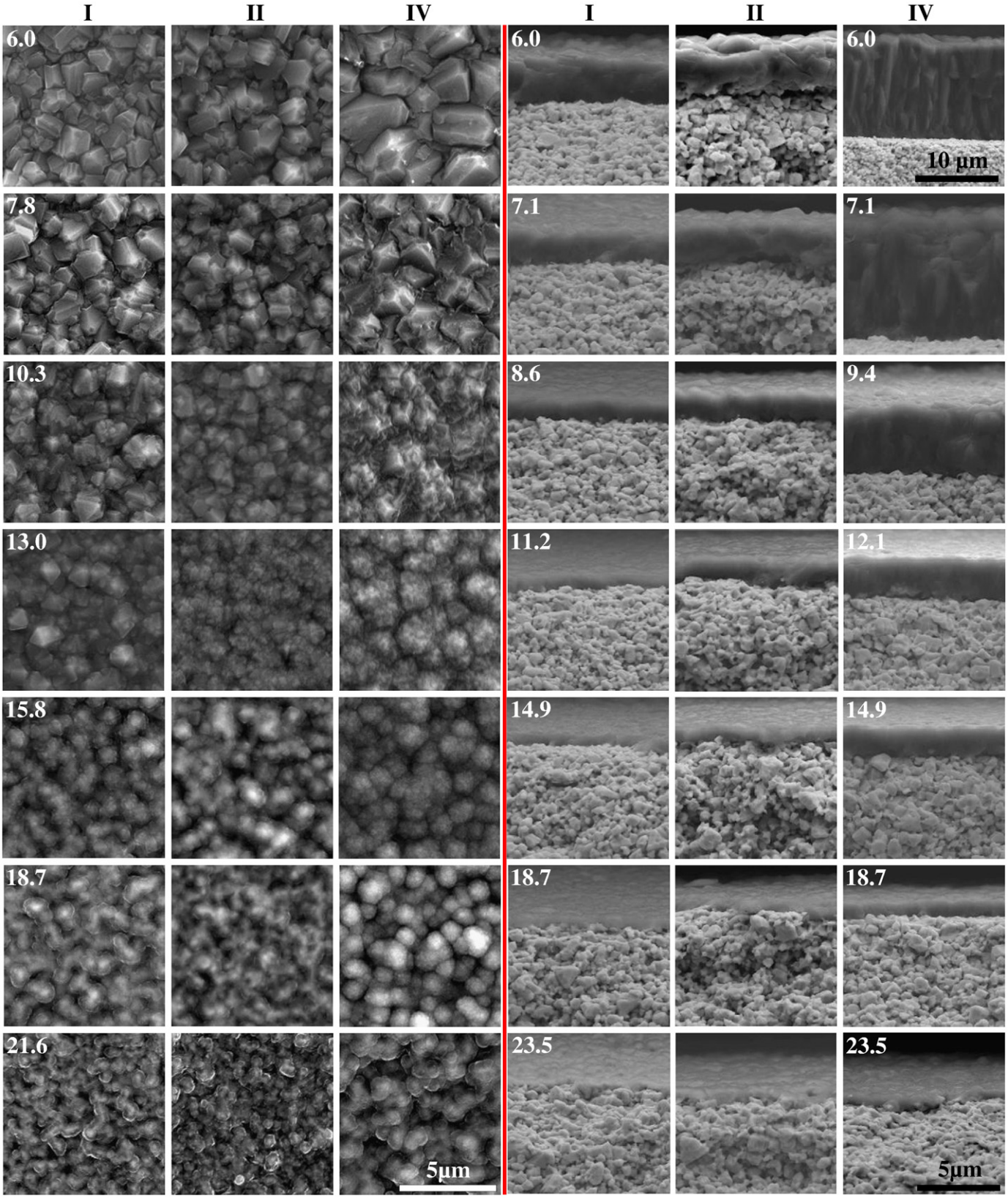

Fig. 2. Representative SEM images of diamond films deposited in this work. The first three columns display surface morphologies of specimens I, II and IV at increasing d_f (in mm, indicated in the top left of the panels in each row) while the final three columns show the corresponding cross sections measured as a function of d_f (in mm).

characterized by Raman spectroscopy, at many different locations on each sample. Fig. 4(a) and (c) show two illustrative Raman spectra taken with specimen IV. As with all other spectra recorded in this work, these spectra show an obvious background that rises to higher wavenumber. This photoluminescence (PL) contribution is fitted using a polynomial function (Y1) as shown in Fig. 4(a) and (c) and then subtracted to yield the Raman contributions, which are then fitted using a set of Lorentzian functions — as shown in Fig. 4(b) and (d).

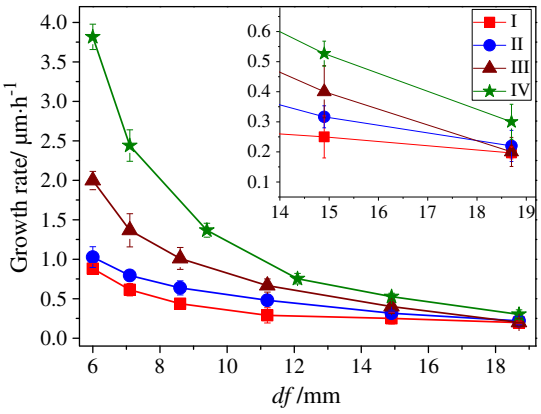

Fig. 3. Growth rates of diamond films (determined by cross-sectional SEM analysis) plotted as a function of d_f, for specimens I, II, III and IV.

Fig. 5 shows such decompositions of the Raman component in spectra recorded at a range of d_f values for each of specimens I–IV. Clearly, the relative intensities of all of the major features (centered at ~1140, 1220, 1332, 1355, 1470 and 1575 cm^{-1}) evolve with increasing d_f and are sensitive to process conditions (both p and the C/H ratio).

Diamond has a face-centered cubic lattice, space group Fd3m. There are two carbon atoms in the primitive unit cell, and thus a single triply degenerate first order phonon with symmetry F_{2g} [16–18]. The single sharp Raman peak at ~1332 cm^{-1} (Fig. 5) is attributable to these F_{2g} modes at the center of the Brillouin zone of the cubic diamond. The prominence (or otherwise) of the ~1332 cm^{-1} feature in the Raman spectra of polycrystalline diamond films is a valuable indicator of the relative sp^3 carbon content (and thus of diamond quality). As Fig. 6 shows, the area of this peak (A_{1332}) declines with increasing d_f, for all four samples, with specimen IV (highest $F(CH_4)$) showing the greatest relative rate of decrease. A rationale for these observations is developed in the following paragraphs.

The peaks of ~1355 cm^{-1} and ~1575 cm^{-1} are both due to Raman scattering from graphite [19]. The Raman spectrum of single crystal graphite shows only one mode, at ~1575 cm^{-1}, assigned to zone center phonons of E_{2g} symmetry of the infinite crystal [19,20]. The band at ~1355 cm^{-1} is not evident in the Raman spectra of large grain single crystals of graphite, but does appear in the spectrum of well crystallized graphite with small particle size [19,21,22]. The presence of small particles of polycrystalline graphite increases the crystalline disorder, and thus the intensity of the disorder-induced features; i.e. they encourage a breakdown of the $q=0$ selection rule, allowing the K-point phonon (A_{1g} symmetry) of the hexagonal Brillouin zone to contribute to the Raman scattering [17,19,21,22]. The bands at ~1355 and ~1575 cm^{-1} (the so-called D and G bands) are the traditional diagnostic for the presence of sp^2 carbon [17,23–27]. Crudely, the G peak can be associated with bond stretching of all pairs of sp^2 atoms in both rings and chains [26], while the D peak can be viewed in terms of breathing modes of sp^2 atoms in rings [27]. Fig. 7(a) serves to highlight the strong correlation between these two peak areas (A_{1355} vs A_{1575}, R^2 ~0.84, see Table 2), for all four samples and at all d_f.

The origin of the two peaks at ~1140 and ~1470 cm^{-1} has been the subject of much debate. The ~1470 cm^{-1} peak cannot be associated

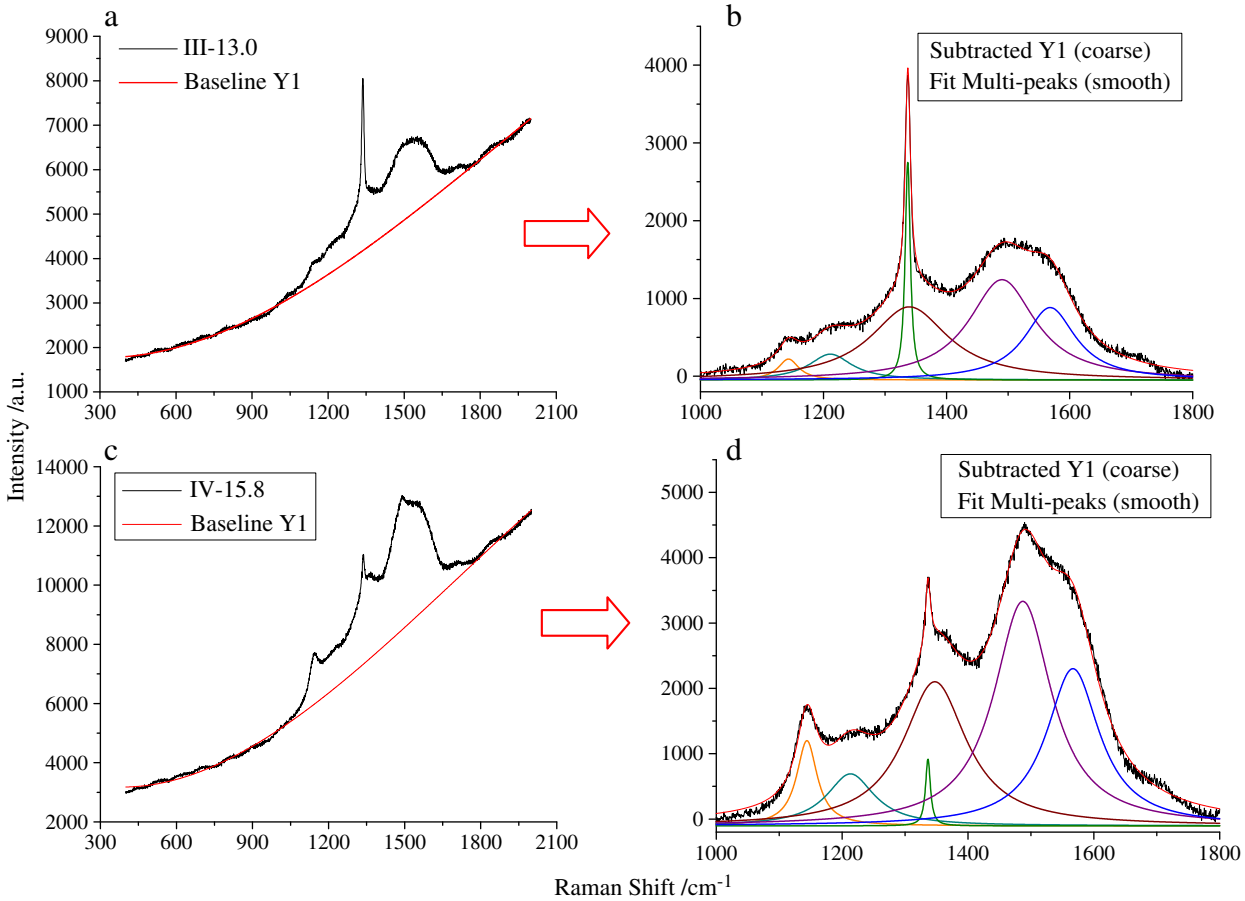

Fig. 4. Raman spectra of diamond films taken at test points on samples III, $d_f=13.0$ mm (a) and IV, $d_f=15.8$ mm (c). The PL background signal (Y1, reproduced with a polynomial function and shown in red) has been subtracted to yield the Raman spectra shown in (b) and (d) which are then fitted using six Lorentzian functions.

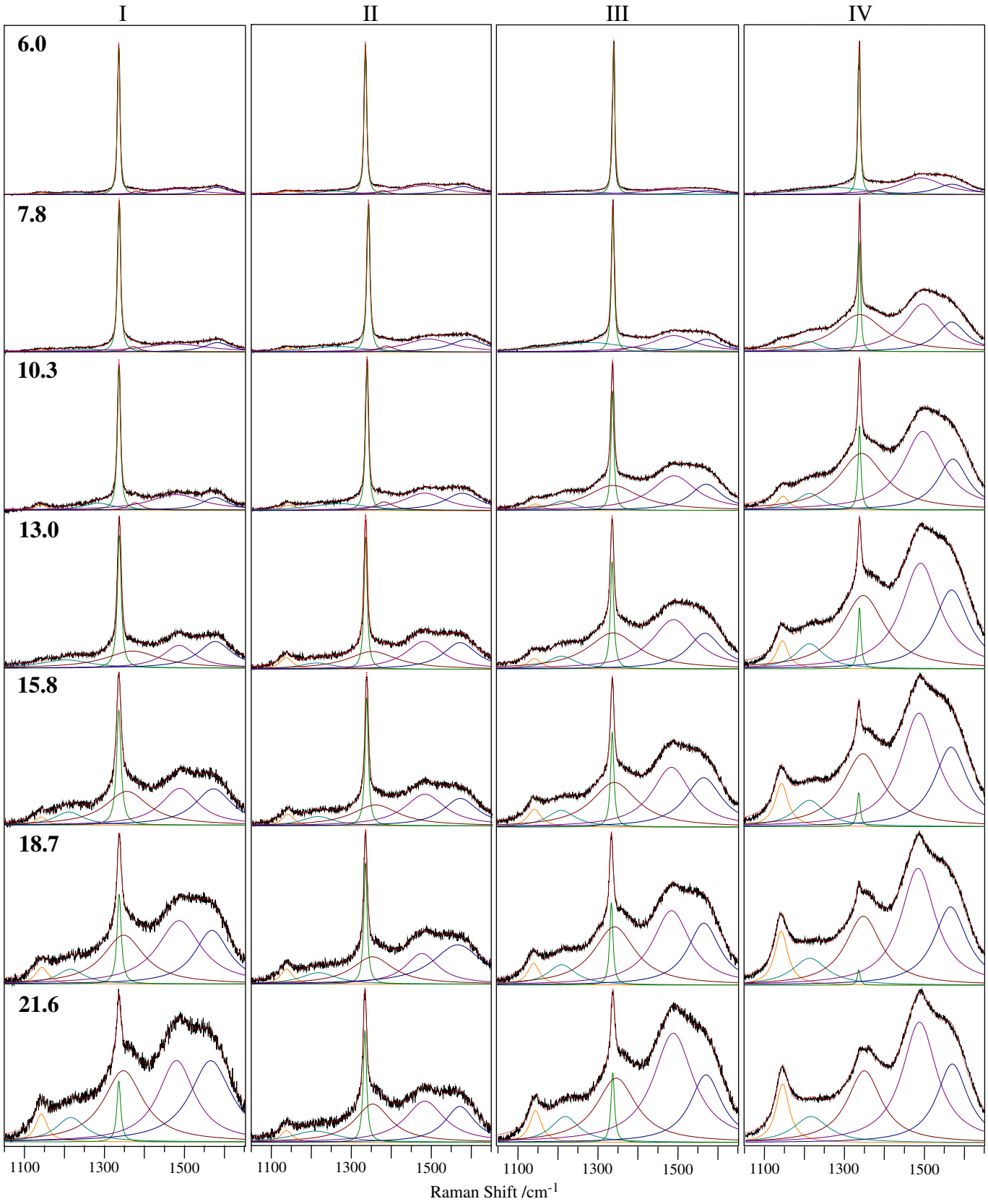

Fig. 5. Raman spectra (after fitting and subtracting the PL background signal) of diamond films deposited at different d_f on specimens I, II, III and IV, along with their decompositions.

with the diamond phase, since the diamond structure does not allow any first order Raman modes at wavenumbers >1332 cm^{-1}, even in the presence of disorder [16,26]. Abello et al. observed a ~1470 cm^{-1} peak in Raman spectra of fullerenes; it is the dominant Raman band of C_{60} [28]. A ~1470 cm^{-1} feature was also observed in the Raman spectra of a fullerene sample that had been partially transformed to diamond by application of high pressure [29,30], and of carbon films grown by pulsed laser evaporation of graphite — where it was linked to five

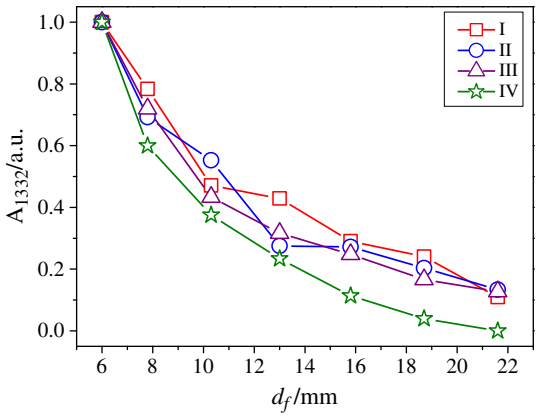

Fig. 6. Plot showing the d_f dependence of the area of the ~1332 cm^{-1} peak in the Raman spectra of specimens I, II, III and IV.

member carbon rings on the basis of companion scanning tunneling microscopy measurements [31]. Analogy with Raman spectra of amorphous and microcrystalline Si led to the suggestion that the ~1140 cm^{-1} feature might be attributable to amorphous or microcrystalline diamond structures [32]. As with the disorder induced broad Raman features attributed to small grain-size crystallized graphite, Nemanich et al. proposed that the $q=0$ selection rule would also be relaxed for sufficiently small grain-size diamond, thereby allowing contributions from phonon modes with $q\neq 0$ [25] — a view supported in several subsequent analyses [33–36]. Alternative assignments, based on polymeric chains like polyenes [37] or trans-polyacetylene [38] have been advanced, however. Ferrari et al. argued that the 1140 cm^{-1} peak cannot be assignable to nanocrystalline diamond (NCD) or other sp^3-bonded phases [18]. These workers recorded Raman spectra from low quality CVD diamond films at a range of excitation wavelengths and found that the ~1140 cm^{-1} and ~1470 cm^{-1} features disperse by 50–100 cm^{-1} as the excitation energy is increased, and decline in relative intensity. The former behavior is incompatible with a density-of-states feature, which should be insensitive to excitation wavelength, while the latter is inconsistent with attribution of these bands to sp^3 sites since, given the wide (5.5 eV) band gap of the sp^3 carbon lattice, the resonance enhancement of sp^3 Raman features should increase with increasing excitation energy — as is indeed observed for the 1332 cm^{-1} feature. sp^2 sites, in contrast, have a low band gap and are most readily excited at visible excitation wavelengths. Such considerations therefore led Ferrari et al. [18] to attribute both the ~1140 and ~1470 cm^{-1} features to trans-polyacetylene segments (the ν_1 and ν_3 modes, respectively), which are likely to be concentrated at grain boundaries and at the surface. Pfeiffer et al. subsequently demonstrated very good agreement between the measured wavenumber of the 1140 cm^{-1} feature from diamond samples grown on a range of substrates and the results of a vibronic model of resonance Raman scattering from trans-polyacetylene [39]. The same group also performed cross-sectional Raman investigations on NCD samples and found that the relative intensity of the ~1140 cm^{-1} peak declines when sampling deeper into the bulk — consistent with a proliferation of trans-$(CH)_x$ species at the surface [40]. Despite this growing body of evidence supporting sp^2 based assignments for the ~1140 cm^{-1} (and ~1470 cm^{-1}) peaks, however, the ~1140 cm^{-1} Raman feature is still often invoked as a signifier of a nanocrystalline diamond phase in as-grown CVD samples [41,42].

The CVD diamond films grown in the present work are derived from four different input gas mixtures, and each specimen contains material grown at a range of d_f (and thus T_s). The spatially resolved Raman data shown in Fig. 5 thus offer a means of testing further (and refining) current interpretations of the Raman spectra of polycrystalline diamond samples. Even a cursory inspection of Fig. 5 reveals that the relative intensity of the ~1140 cm^{-1} peak increases with increasing d_f and with increasing $F(CH_4)$, and that the trends in the ~1140 cm^{-1} peak area are mirrored by the ~1470 cm^{-1} peak . This trend is quantified in Fig. 7(b): the correlation between the ~1140 cm^{-1} and ~1470 cm^{-1} peak areas (A_{1140} vs A_{1470}, R^2 ~0.63, Table 2) supports the view that these two features share a common carrier. Having established the A_{1355}/A_{1575} and A_{1140}/A_{1470} pair correlations (Fig. 7(a) and (b)), Fig. 7(c) compares the relative areas of one feature from each pair in each of the Raman spectra (A_{1470} vs A_{1575}, R^2 ~0.93, see Table 2) while Fig. 7(d) highlights the obvious anti-correlation between both of these peak areas and those of the corresponding 1332 cm^{-1} (sp^3) peaks (R^2 ~0.00 and 0.04, respectively, as shown in Table 2). The present analysis thus clearly favors assignment of the ~1140 cm^{-1} and ~1470 cm^{-1} features to sp^2 carbon based structures.

The present fitting procedures return an additional feature centered at ~1220 cm^{-1}, the relative importance of which appears to scale with that of the other sp^2-based features. May et al. [43,44] identified a feature at similar wavenumber in the Raman spectra of B-doped polycrystalline films, which they tentatively attributed to a Fano resonance with the 1332 cm^{-1} (sp^3) feature. Prawer et al. [45] have suggested that a broad feature identified at ~1250 cm^{-1} in the Raman spectrum of nanophase diamond powder could have an sp^3 origin, and a similar feature seen in the Raman spectra of NCD films has been tentatively ascribed to amorphous sp^3-bonded carbon [46]. Analysis of the present Raman spectra points to a contrary interpretation, however. Correlating the areas of the ~1220 cm^{-1} feature with that of the ~1575 cm^{-1} (a signifier of sp^2 carbons) and the ~1332 cm^{-1} (sp^3 carbon) peaks in each of the measured Raman spectra returns R^2 coefficients of 0.91 and 0.02 (Fig. 7(e) and (f), respectively, see Table 2), suggesting that sp^2 carbons are much more likely to be the carrier of the ~1220 cm^{-1} feature.

3.3. Raman shift and residual stress

Fig. 8 shows the d_f dependences of the center wavenumbers of both the ~1332 cm^{-1} (sp^3) and ~1575 cm^{-1} (sp^2 (G)) peaks returned by fitting the measured Raman spectra for each specimen. The wavenumbers of the first-order Raman peak of diamond and related sp^3-carbon materials [47–50] and of the G peak of graphite (and related sp^2-carbon materials) [51–53] both increase near-linearly with increasing pressure loading (i.e. with increased compressive stress). Ralchenko et al. [54] have proposed the following relationship between the wavenumber shift $\Delta\tilde{\nu}$ and stress, σ, for polycrystalline diamond films:

$$\sigma[\mathrm{GPa}] = -0.567\left[\mathrm{GPa}/\mathrm{cm}^{-1}\right]\Delta\tilde{\nu}\left[\mathrm{cm}^{-1}\right] \quad (1)$$

where $\Delta\tilde{\nu}=\tilde{\nu}_m-\tilde{\nu}_0$ is the difference between the measured peak wavenumber ($\tilde{\nu}_m$) and the unperturbed line center wavenumber ($\tilde{\nu}_0=1332\ cm^{-1}$). As Fig. 8(a) shows, $\Delta\tilde{\nu}$ is consistently positive for the polycrystalline diamond material grown in this work but decreases with increasing d_f and, for any given d_f, is consistently larger for the thicker films (*e.g.* specimens III and IV). Such observations are consistent with the view that the diamond component within the deposited films has inherent compressive stress. This can be traced, primarily, to the different thermal expansion coefficients of the polycrystalline diamond and the underlying substrate. $\Delta\tilde{\nu}$ thus tends to be highest in the thicker, higher quality material (*e.g.* specimen III at small d_f), recall Fig. 5-III 6.0. The decline in $\Delta\tilde{\nu}$ with increasing d_f can be understood both in terms of the lower T_s prevailing at higher d_f, and the increasing sp^2 content of films grown at larger d_f — which affords some stress relief. Hanfland et al. [51] measured Raman spectra and lattice parameters of hexagonal graphite at pressures up to the structural phase transition near 14 GPa

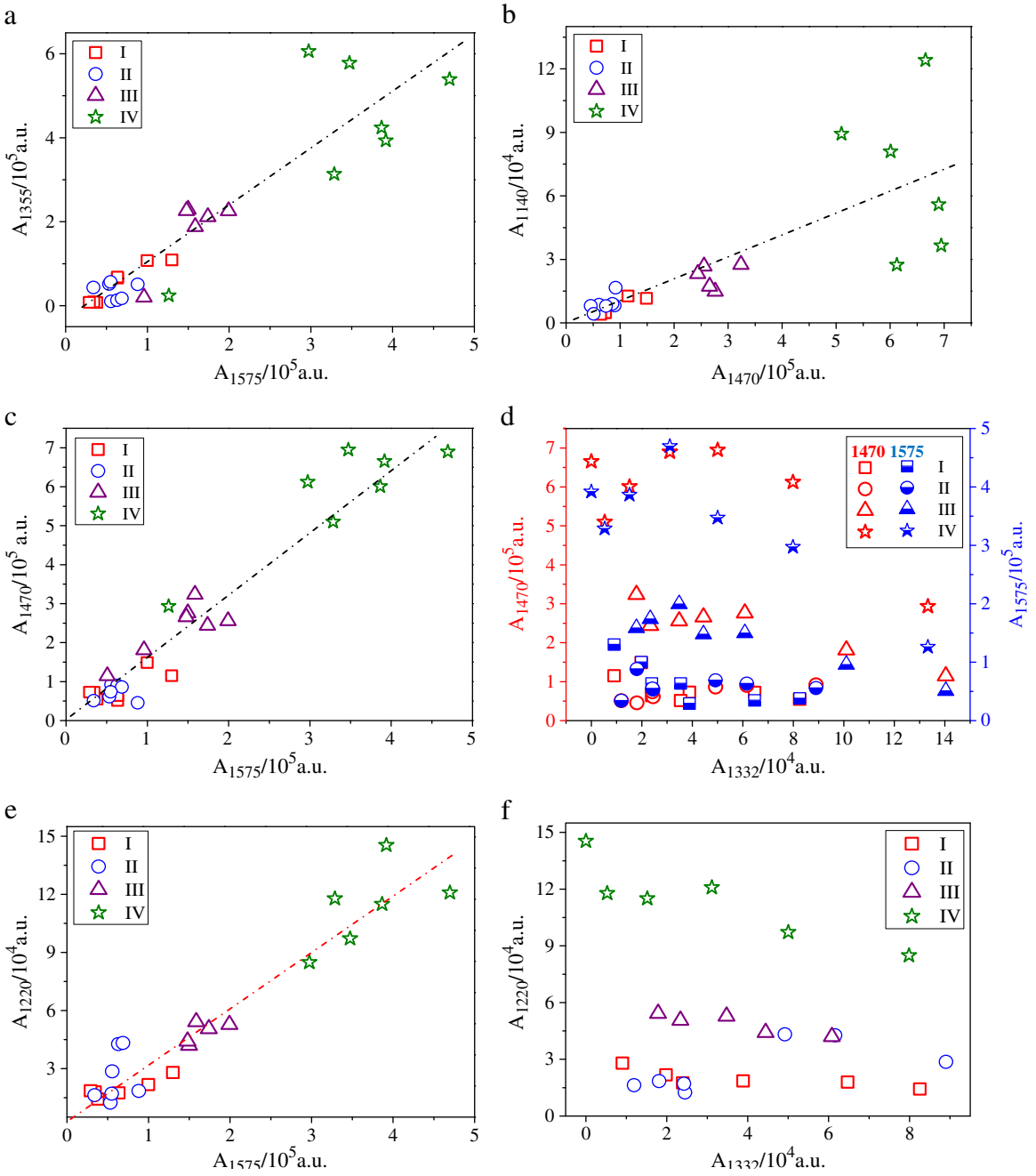

Fig. 7. Correlations between areas of selected pairs of peaks in Raman spectra of diamond films grown in the present study: (a) A_{1355} vs A_{1575}, (b) A_{1140} vs A_{1470}, (c) A_{1470} vs A_{1575}, (d) A_{1470} and A_{1575} vs A_{1332}, (e) A_{1220} vs A_{1575}, and (f) A_{1220} vs A_{1332}.

($T = 300$ K), and found the wavenumber of the E_{2g} in-plane mode to increase with an initial pressure coefficient of 4.7 cm^{-1}/GPa. The stress-induced shift of the G peak in Raman spectra of sp^2 carbon materials is therefore typically parameterized as [52,53]

$$\Delta\tilde{\nu} = (\tilde{\nu}_m - \tilde{\nu}_0)\left[cm^{-1}\right] = 5\left[cm^{-1}/GPa\right] \times \sigma[GPa] \quad (2)$$

with $\tilde{\nu}_0$ variously taken as 1577 and 1579 cm^{-1} [51–53]. Irrespective of the precise value assumed for $\tilde{\nu}_0$, it is clear from Fig. 8(b) that $\Delta\tilde{\nu}$ is positive only in the case of the thinnest samples grown at small d_f and that, for these films in particular, $\Delta\tilde{\nu}$ declines markedly with increasing d_f. Based on such analysis, we might conclude that, in all cases, the sp^2 carbon material grown at large d_f is under tensile stress. This might be understandable by assuming transmission of stress across the substrate–film interface and noting that, in the case of graphite/WC, it is the graphite that has the large coefficient of thermal expansion ($\alpha(WC) = 4.42\times10^{-6}\,K^{-1}$ (0–100 °C), $\alpha(\text{graphite}) = 25\times10^{-6}\,K^{-1}$ (25–500 °C), *cf* $\alpha(\text{diamond}) = 0.8\times10^{-6}\,K^{-1}$ (25–500 °C) [1]). But the sp^2-bonded carbons in the present films will be predominantly at the grain boundaries [55], not in the form of extended graphite sheets. The diamond component within the deposited films has inherent compressive stress (see Fig. 8(a)). so the sp^2-bonded carbons at the grain boundaries are more likely to be under compressive stress, too. Ferrari et al. used a phenomenological three-stage model (stage 1: from graphite to nanocrystalline graphite; stage 2: from nanocrystalline graphite to *a*-C (amorphous carbon with a significant fraction of sp^3 bonds); and stage 3: from *a*-C to *ta*-C (tetrahedral amorphous carbon with higher sp^3 content)) to interpret the large amount of experimental data on Raman spectra on

Table 2
Correlation (R^2) coefficients returned by fitting the relative areas of selected pairs of features in the decomposed Raman spectra measured for specimens I–IV, over all d_f, to the linear function $y = mx + c$.

Pair correlation		Equation: $y = mx + c$
Peak1	Peak 2	R^2
1140	1332	0.14
1140	1220	0.84
1140	1470	0.63
1140	1575	0.69
1220	1332	0.02
1220	1470	0.89
1220	1575	0.91
1332	1470	−0.02
1332	1575	0.05
1355	1575	0.84
1470	1575	0.93

amorphous carbons excited with visible wavelengths [26]. They considered the introduction of a series of defects: bond-angle disorder, bond-length disorder, and hybridization. The Raman spectrum was considered to depend on clustering of the sp^2 phase, bond disorder, the presence of sp^2 rings or chains, and the sp^2/sp^3 ratio. The main effects in the evolution of the Raman spectrum in their stage 3 are coincident with the results of the present work, i.e. the wavenumber of the *G* peak increases from ~1510 to ~1570 cm^{-1} (or to ~1630 cm^{-1} for sp^2 dimers in ion-implanted diamond), the I(*D*)/I(*G*) ratio of peak heights decreases (to a very low value). These effects have been rationalized in terms of increasing sp^3 content, reflecting the increasing tendency for the sp^2 material to be present as olefinic groups rather than rings. Olefinic C C bonds are shorter than aromatics bonds, and thus have higher vibration frequencies (lying above the band limit of graphite).

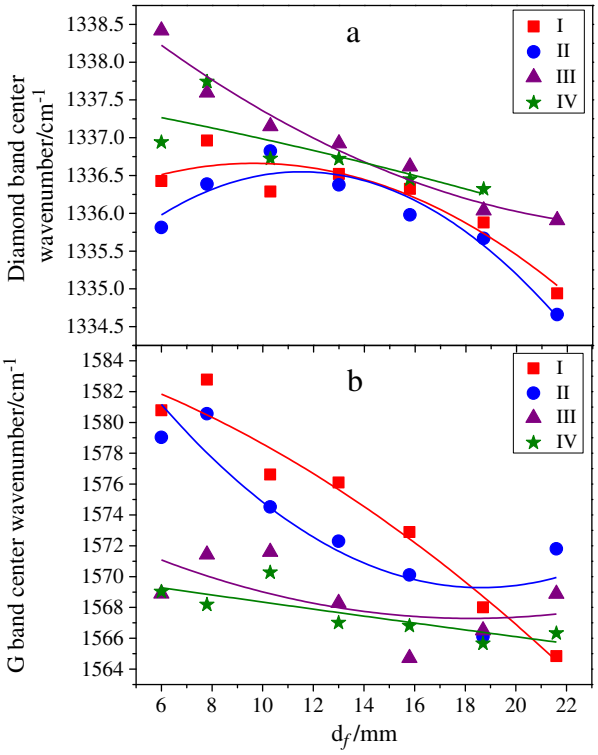

Fig. 8. Plot showing the d_f dependence of the center wavenumber for the ~1332 cm^{-1} band and the *G* band after decomposition of the Raman spectra of specimens I, II, III and IV.

3.4. Correlating diamond film properties with the local gas phase composition

To simplify three-dimensional (3-D) modeling of the gas phase chemistry and composition within the present work the HF is treated as a single wire, with its long axis aligned perpendicular to the major axis of the largest surface of the bar substrate. Cartesian coordinates (*x*, *y*, and *z*) are used. The *z* axis is perpendicular to the filament and coincident with the major axis bisecting the largest face of the bar substrate, the filament axis is along *y*, and *x* is perpendicular to both the HF axis and the major center axis of the bar substrate, as shown in Fig. 9. The point (0, 0, 0) corresponds to a top of this major center axis, which is 6 mm below the bottom of the HF. The line ($x = 0$, $z = -7$ mm, *y*) corresponds to the wire axis. The orientation of the bar substrate in the modeling aligned along the *z* axis – because of the symmetry conditions required in the 3-D model code – differs from the experimental arrangement (at ~30° to the *z* axis), but we do not consider that this difference significantly compromises the comparison between the experimental and calculated results. The reactive gas mixture flows parallel to *z*, through the filament to the substrate. The coiled region of the HF was treated as the hot (active) region in the modeling, so the effective surface area supporting H atom production was calculated as $S = L \times C = 72.5$ mm^2, where L ~60 mm is the length of wire in the coiled region and C ~1.2 mm is the girth of the filament.

The 3-D model has been described previously [9,11,12] and consists of three blocks that describe, respectively, gas phase processes (heat and mass transfer, chemical kinetics), gas-surface processes at the substrate (diamond growth mechanism), and the processes of a reactive mixture (gas heating, catalytic hydrogen dissociation at the filament). H_2 molecules dissociate at the HF surface [56] and the resulting H atoms diffuse throughout the reactor volume. The lack of efficient H atom loss processes in dilute CH_4/H_2 gas mixtures such as those used in the present work ensures that H atom densities in the cooler periphery of the reactor are far in excess of those expected on the basis of local thermodynamic equilibrium. H atoms drive the inter-conversion between C_1 (CH_y) and C_2 (C_2H_x) species — both via the families of radical forming (so-called 'H-shifting') abstraction reactions and, in the cooler regions, by a sequence of third-body stabilized H addition reactions that culminate in the conversion of C_2H_x species to members of the CH_y family [57]. The temperature discontinuity ΔT near the HF (i.e. the difference

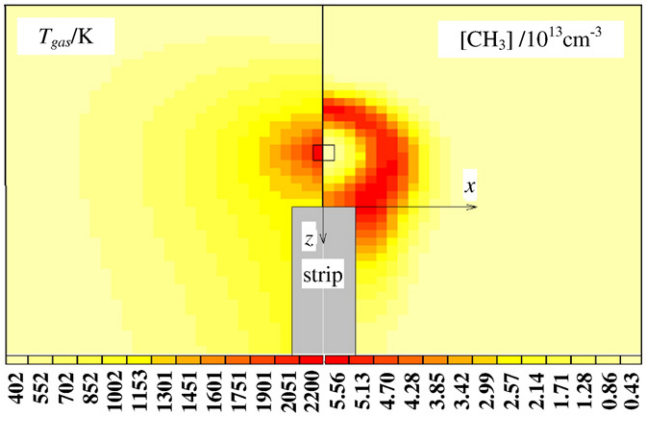

Fig. 9. Calculated distributions of the gas temperature (left) and CH_3 concentration in the plane ($x, z, y = 0$) for base conditions for specimen II, $T_f = 2483$ K, T_s ranging from 1100 K (top)–880 K (bottom), $p = 15.2$ Torr, 1%CH_4/H_2 gas mixing ratio, distance from wire coils to the top of the bar substrate = 6 mm, and the cell size in the color grid = 1 mm × 1 mm. The coiled wire replicating the HF is located inside the square in the center of the 2D image. The color scale increases in 13 equal intervals from the edge of the chamber to the center, i.e. from 253–402 to 2051–2200 K (left), and from 0–0.43 × 10^{13} to 5.13 × 10^{13}–5.56 × 10^{13} cm^{-3} (right).

between the filament temperature and the gas temperature near the filament surface ($\Delta T = T_f - T_{nf}$) was estimated using the Smoluchowski formula and accommodation coefficients from ref. [58]. This analysis yielded ΔT [K] $\approx 570/p$[kPa] (where p is the gas pressure), and this relationship was assumed in the subsequent modeling, which was carried out for the experimental parameters associated with depositions on each of specimens I–IV (detailed in Table 1). The false color plot displayed in Fig. 9 shows the calculated distributions of the gas temperature and the CH_3 number density in the plane (x, z, $y = 0$) for the conditions used in deposition II, while Fig. 10 shows the calculated number density profiles for some of the key reactive species (H and C atoms, and CH_3 radicals) 0.5 mm above the substrate surface (i.e. along the line ($x = 3.5$ mm, $-9 < z < 19$ mm, $y = 0$)) for each of deposition conditions I–IV.

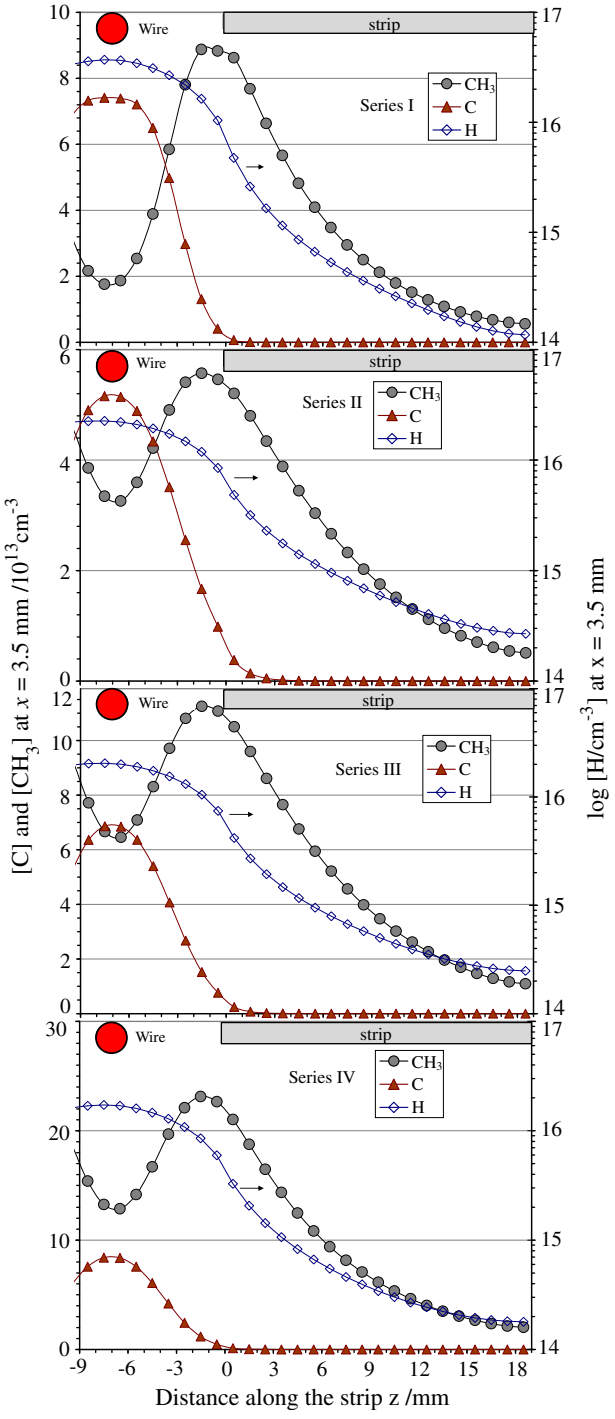

Fig. 10. Calculated concentration profiles of the H and C atoms, and CH_3 radicals, 0.5 mm from the substrate surface (i.e. along the line ($x = 3.5$ mm, $-9 < z < 19$ mm, $y = 0$)) for deposition conditions I–IV.

The effects of the substrate surface ($x = 3.5$ mm, $0 < z < 19$ mm) and of the hot wire surface ($x < 0.9$ mm, $-7.9 < z < -6.1$ mm) on these radical number densities are clearly evident in these plots. The H atom concentration drops as a result of H abstraction and H addition reactions at the substrate (i.e. heterogeneous recombination of H atoms on the substrate surface), and CH_3 radicals are converted to smaller CH_x<3 species (*e.g.* C atoms) by a sequence of H-shifting reactions in the hot near filament region. To link these and all other calculated species number density distributions as functions of height above the substrate with the experimental data we note that, to a good approximation, the experimental distance d_f is related to the model z coordinate by $d_f \approx z + 6$ mm. Fig. 11 shows the calculated variations of T_{gas} and the [H]/[CH_x] ratio (where [H] and [CH_x] are respectively the H atom concentration and the sum of the CH_x species ($x = 0$–3) concentrations) as a function of z at $x = 3.5$ mm (i.e. at 0.5 mm above the substrate surface). T_{gas} falls essentially linearly with increasing d_f but, for a given set of process conditions, the [H]/[CH_x] ratio remains relatively flat once $z > 3$ mm. May et al. [59] have previously argued for a correlation between the [H]/[CH_x] ratio and the resulting CVD diamond film properties, but any such correlation in the present case is likely to be reduced by the variation in T_s within each sample.

Fig. 12 shows the growth rates G predicted using the following equation:

$$G\,[\mu\text{m/h}] = 0.075 \times 3.8 \times 10^{-14} T_s^{0.5} [CH_x] \,/\, \{1 + 0.3 \exp(3430/T_s) + 0.1 \exp(-4420/T_s)\,[H_2]/[H]\}, \quad x = 0\text{–}3 \tag{3}$$

presented in recent kinetic Monte Carlo studies of CVD diamond growth [44,59]. The current modeling indicates that [CH_x]~[CH_3] for the HF activated CH_4/H_2 mixtures used in the present experiments; simple visual comparison of Fig. 12 and the measured growth rates shown in Fig. 3 suffices to demonstrate the good agreement between both the absolute calculated value and the profile of $G(z)$ and the growth parameters determined experimentally at $G(d_f \sim z + 6\text{ mm})$, for all four process conditions.

4. Conclusions

This paper describes a systematic study of polycrystalline diamond film growth by HF-CVD on WC-Co bar substrates using different CH_4/H_2 source gas mixing ratios and two different total gas pressures. Each substrate was mounted so as to span a range of HF-substrate distances ($6.0 \le d_f \le 21.6$ mm) which results in a temperature gradient across the substrate and thus a gradation in the gas phase chemistry and

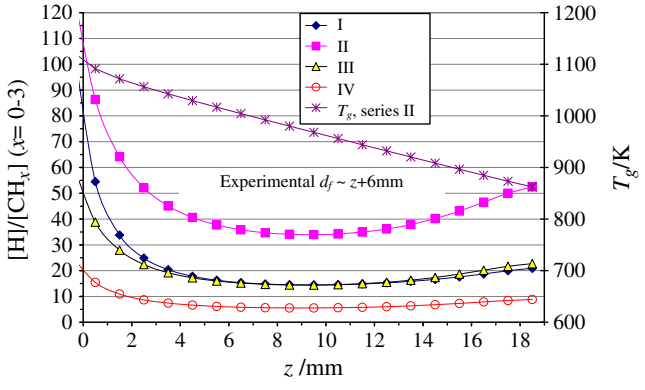

Fig. 11. Plot showing calculated [H]/[CH_x] ratios and gas temperature $T_{gas,II}$ at a distance 0.5 mm from the substrate (i.e. along the line ($x = 3.5$ mm, $-9 < z < 19$ mm, $y = 0$)). [CH_x] is the sum of the various CH_x ($x = 0$–3) species concentrations.

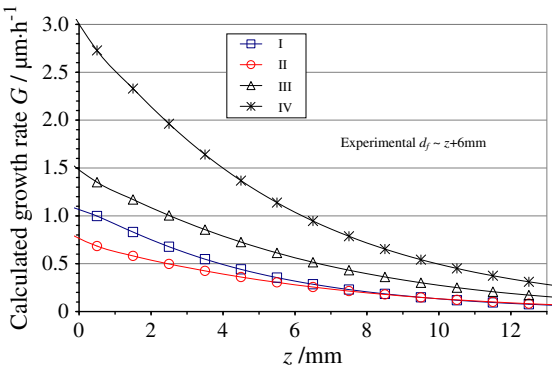

Fig. 12. Calculated growth rate G (in μm/h), plotted as a function of *z*.

composition present at the substrate surface. Spatially resolved SEM and Raman analysis of the deposited material has provided a detailed picture of the d_f dependence of the film morphology, growth rate (G), sp^3/sp^2 content and stress, for each specimen, and of how these properties vary with process conditions. The surface morphology of the deposited film is seen to evolve from that characteristic of dense, homogeneous, well-facetted, polycrystalline diamond film (at d_f ~6 mm), through a 'cauliflower'-like morphology (at d_f ~10–12 mm), to an agglomeration of quasi-spherical nanoscale particles at large d_f. The growth rate G falls with increasing d_f under all process conditions, scales roughly linearly with $F(CH_4)$ at small d_f (~6 mm) but is rather insensitive to $F(CH_4)$ at large d_f. Neither the surface morphology nor G is particularly sensitive to the process gas pressure. The measured Raman spectra are analyzed in terms of six overlapping Lorentzian features, centered at ~1140, ~1220, ~1332, ~1355, ~1470 and ~1575 cm^{-1}, with relative weightings that are found to vary with d_f and with process conditions. The assignments of three of these – the ~1332, ~1355 and ~1575 cm^{-1} bands – are incontrovertible (to diamond, and to the so-called *D* and *G* bands of graphitic carbon, respectively). Investigating the correlation between different pairs of features across the whole range of sample and d_f space leads to the conclusion that the ~1140 cm^{-1}, ~1220 cm^{-1} and ~1470 cm^{-1} features are all carried by sp^2 carbon based structures. The experimental study is complemented by two-dimensional model calculations of the HF-activated gas phase chemistry and composition in the vicinity of the substrate surface which succeed in reproducing the measured growth rates and their d_f dependences well.

Acknowledgements

The authors wish to thank the "China Scholarship Council", the "State Key Laboratory of Powder Metallurgy", the "Outstanding PhD Students Enabling Fund", the "Innovation Foundation for Postgraduates of Hunan Province of China", and the "Open Fund for Valuable Instruments of Central South University" for financial support. The Bristol–Moscow collaboration is supported by a Royal Society Joint Project Grant, and Y.A.M. acknowledges support from the RF Government for Key Science, schools grant no. 3322.2010.2.

References

[1] H. Liu, D.S. Dandy, Diam Relat Mater 4 (1995) 1173.
[2] S. Ferro, J. Mater. Chem. 12 (2002) 2843.
[3] M.N.R. Ashfold, P.W. May, C.A. Rego, N.M. Everitt, Chem. Soc. Rev. 23 (1994) 21.
[4] D. Das, R.N. Singh, Internat. Mater. Rev. 52 (2007) 29.
[5] R.S. Balmer, J.R. Brandon, S.L. Clewes, H.K. Dhillon, J.M. Dodson, I. Friel, P.N. Inglis, T.D. Madgwick, M.L. Markham, T.P. Mollart, N. Perkins, G.A. Scarsbrook, D.J. Twitchen, A.J. Whitehead, J.J. Wilman, S.M. Woollard, J. Phys. Condensed Matter 21 (2009) 364221.
[6] Q. Wei, Z.M. Yu, M.N.R. Ashfold, Z. Chen, L. Wang, L. Ma, Surf. Coat. Tech. 205 (2010) 158.
[7] Q.P. Wei, Z.M. Yu, L. Ma, D.F. Yin, J. Ye, Appl. Surf. Sci. 256 (2009) 1322.
[8] Q.-p. Wei, Z.M. Yu, M.N.R. Ashfold, J. Ye, L. Ma, Appl. Surf. Sci. 256 (2010) 4357.
[9] Y.A. Mankelevich, A.T. Rakhimov, N.V. Suetin, Diam Relat Mater 4 (1995) 1065.
[10] Y.A. Mankelevich, A.T. Rakhimov, N.V. Suetin, Diam Relat Mater 5 (1996) 888.
[11] Y.A. Mankelevich, A.T. Rakhimov, N.V. Suetin, Diam Relat Mater 7 (1998) 1133.
[12] Y.A. Mankelevich, N.V. Suetin, M.N.R. Ashfold, J.A. Smith, E. Cameron, Diam Relat Mater 10 (2001) 364.
[13] M.N.R. Ashfold, P.W. May, J.R. Petherbridge, K.N. Rosser, J.A. Smith, Y.A. Mankelevich, N.V. Suetin, Phys. Chem. Chem. Phys. 3 (2001) 3471.
[14] M.G. Peters, R.H. Cummings, European Patent A1 (1992) 0519587
[15] M. Amaral, A.J.S. Fernandes, M. Vila, F.J. Oliveira, R.F. Silva, Diam Relat Mater 15 (2006) 1822.
[16] S.A. Solin, A.K. Ramdas, Phys. Rev. B 1 (1970) 1687.
[17] D.S. Knight, W.B. White, J. Mater. Res. 4 (1989) 385.
[18] A.C. Ferrari, J. Robertson, Phys. Rev. B 63 (2001) 121405.
[19] F. Tuinstra, J.L. Koenig, J. Chem. Phys. 53 (1970) 1126.
[20] N. Wada, S.A. Solin, Phys. B 105 (1981) 353.
[21] R.J. Nemanich, S.A. Solin, Phys. Rev. B 20 (1979) 392.
[22] P. Lespade, R. Aljishi, M.S. Dresselhaus, Carbon 20 (1982) 427.
[23] R.O. Dillon, J.A. Woollam, V. Katkanant, Phys. Rev. B 29 (1984) 3482.
[24] P. Lespade, A. Marchand, M. Couzi, F. Cruege, Carbon 22 (1984) 375.
[25] R.E. Shroder, R.J. Nemanich, J.T. Glass, Phys. Rev. B 41 (1990) 3738.
[26] A.C. Ferrari, J. Robertson, Phys. Rev. B 61 (2000) 14095.
[27] A.C. Ferrari, J. Robertson, Phys. Rev. B 64 (2001) 075414.
[28] L. Abello, N. Rosman, F. Genet, G. Lucazeau, J. Phys. IV 1 (1991) 497.
[29] M.N. Regueiro, L. Abello, G. Lucazeau, J.L. Hodeau, Phys. Rev. B 46 (1992) 9903.
[30] M. Nunezregueiro, J.L. Hodeau, L. Abello, G. Lucazeau, Diam Relat Mater 2 (1993) 1203.
[31] J. Diaz, J.A.M. Gago, S. Ferrer, F. Comin, L. Abello, G. Lucazeau, Diam Relat Mater 1 (1992) 824.
[32] R.J. Nemanich, J.T. Glass, G. Lucovsky, R.E. Shroder, J. Vac. Sci. Technol. A 6 (1988) 1783.
[33] W.A. Yarbrough, R. Messier, Science 247 (1990) 688.
[34] S.R.P. Silva, G.A.J. Amaratunga, E.K.H. Salje, K.M. Knowles, J. Mater. Sci. 29 (1994) 4962.
[35] M. NishitaniGamo, T. Ando, K. Yamamoto, K. Watanabe, P.A. Dennig, Y. Sato, M. Sekita, Appl. Phys. Lett. 70 (1997) 1530.
[36] L.C. Nistor, J. Van Landuyt, V.G. Ralchenko, E.D. Obraztsova, A.A. Smolin, Diam Relat Mater 6 (1997) 159.
[37] A. Baruya, D.L. Gerrard, W.F. Maddams, Macromolecules 16 (1983) 578.
[38] I. Harada, Y. Furukawa, M. Tasumi, H. Shirakawa, S. Ikeda, J. Chem. Phys. 73 (1980) 4746.
[39] R. Pfeiffer, H. Kuzmany, P. Knoll, S. Bokova, N. Salk, B. Günther, Diam Relat Mater 12 (2003) 268.
[40] H. Kuzmany, R. Pfeiffer, N. Salk, B. Gunther, Carbon 42 (2004) 911.
[41] X.M. Meng, S.J. Askari, W.Z. Tang, L.F. Hei, F.Y. Wang, C.S. Jiang, F.X. Lu, Vacuum 82 (2008) 543.
[42] A. Schneider, D. Steinmueller-Nethl, M. Roy, F. Franek, Int. J. Refract. Met. H. Mater. 28 (2010) 40.
[43] P.W. May, W.J. Ludlow, M. Hannaway, P.J. Heard, J.A. Smith, K.N. Rosser, Chem. Phys. Lett. 446 (2007) 103.
[44] P.W. May, Y.A. Mankelevich, J. Phys. Chem. C 112 (2008) 12432.
[45] S. Prawer, K.W. Nugent, D.N. Jamieson, J.O. Orwa, L.A. Bursill, J.L. Peng, Chem. Phys. Lett. 332 (2000) 93.
[46] R. Mills, J. Sankar, A. Voigt, J. He, P. Ray, B. Dhandapani, Thin Solid Films 478 (2005) 77.
[47] F. Cerdeira, C.J. Buchenau, F.H. Pollak, M. Cardona, Phys. Rev. B 5 (1972) 580.
[48] M.H. Grimsditch, E. Anastassakis, M. Cardona, Phys. Rev. B 18 (1978) 901.
[49] H. Boppart, J. Vanstraaten, I.F. Silvera, Phys. Rev. B 32 (1985) 1423.
[50] S.K. Sharma, H.K. Mao, P.M. Bell, J.A. Xu, J. Raman Spectrosc. 16 (1985) 350.
[51] M. Hanfland, H. Beister, K. Syassen, Phys. Rev. B 39 (1989) 12598.
[52] A. Heiman, E. Lakin, E. Zolotoyabko, A. Hoffman, Diam Relat Mater 11 (2002) 601.
[53] S.C. Ramos, A.F. Azevedo, M.R. Baldan, N.G. Ferreira, J. Vac. Sci. Technol. A 28 (2010) 27.
[54] V.G. Ralchenko, A.A. Smolin, V.G. Pereverzev, E.D. Obraztsova, K.G. Korotoushenko, V.I. Konov, Y.V. Lakhotkin, E.N. Loubnin, Diam Relat Mater 4 (1995) 754.
[55] A. Erdemir, M. Halter, G.R. Fenske, A.R. Krauss, D.M. Gruen, S.M. Pimenov, V.I. Konov, Surf. Coat. Tech. 91–95 (1997) 537.
[56] D.W. Comerford, U.F.S. D'Haenens-Johansson, J.A. Smith, M.N.R. Ashfold, Y.A. Mankelevich, Thin Solid Films 516 (2008) 521.
[57] J.E. Butler, Y.A. Mankelevich, A. Cheesman, J. Ma, M.N.R. Ashfold, J. Phys. Condensed Matter 21 (2009) 364201.
[58] A.D. Terekhov, N. Frolova, Z. Prikl. Mekhaniki I Tekhnicheskoi Fiziki 4 (1972) 173.
[59] P.W. May, J.N. Harvey, N.L. Allan, J.C. Richley, Y.A. Mankelevich, J. Appl. Phys. 108 (2010) 014905.